

Technical Notes

Optical Diagnostics for Characterizing a Transitional Shear Layer over a Supersonic Cavity

Michael J. Hargather* and Gary S. Settles†
Pennsylvania State University, University Park,
Pennsylvania 16802
and
Sivaram Gogineni‡
Spectral Energies, LLC, Dayton, Ohio 45431

DOI: 10.2514/1.J052421

I. Introduction

C AVITY flowfields have been the subject of research since the 1950s, and still remain the subject of active research. The basic mechanisms governing cavity flows were first described by Rossiter [1], but a detailed understanding of the complete flow physics still does not exist. A wide variety of experimental investigations into cavity flowfields have been presented, including subsonic [2,3] and supersonic [4,5] freestream velocities. A detailed review of cavity research efforts was recently given by Cattafesta et al. [6].

Refractive imaging optical diagnostic techniques, such as schlieren and shadowgraphy [7], have been an important part of cavity experimental investigations. Rossiter used shadowgraph imaging in his original work to identify shock-wave structures and general motions [1]. Schlieren optics and photodiodes (schlieren deflectometry [7]) were used by Cattafesta et al. [2] and Garg and Cattafesta [8] to measure the density fluctuations and the frequency content at locations in a cavity shear layer. Zhuang et al. [4,9] have used schlieren images to supplement pressure and particle-image-velocimetry (PIV) measurements over a supersonic cavity. A recent study by Alvi and Cattafesta has reviewed the range of flow-visualization techniques that have been used for cavity-flow-control experiments [10].

The present work applies high-speed digital shadowgraph, and focusing schlieren imaging to the study of a supersonic cavity flowfield. A range of analyses are presented, including new image-processing techniques for examining a transient flow, a frequency analysis similar to that described in other investigations [2,11], and schlieren image velocimetry (SIV) [12].

Received 2 November 2012; revision received 14 May 2013; accepted for publication 11 June 2013; published online 8 October 2013. Copyright © 2013 by the American Institute of Aeronautics and Astronautics, Inc. All rights reserved. Copies of this paper may be made for personal or internal use, on condition that the copier pay the \$10.00 per-copy fee to the Copyright Clearance Center, Inc., 222 Rosewood Drive, Danvers, MA 01923; include the code 1533-385X/13 and \$10.00 in correspondence with the CCC.

*currently Assistant Professor, New Mexico Tech, Mechanical Engineering Department, 801 Leroy Place, Socorro, New Mexico 87801. Member AIAA.

†Distinguished Professor of Mechanical Engineering, Department of Mechanical and Nuclear Engineering, 301D Reber Building, Associate Fellow AIAA.

‡President, 5100 Springfield Street, Suite 301. Fellow AIAA.

II. Experimental Methods

The experiments reported here were performed at the U.S. Air Force Research Laboratory Trisonic Gasdynamics Facility (TGF) at Wright-Patterson Air Force Base. This closed-loop continuous-flow facility operates at a constant stagnation temperature of 297 ± 2 K, variable stagnation pressure with a maximum dynamic pressure of 50 kPa, and a maximum supersonic Reynolds number of $1.6 \cdot 10^7/m$. The test section is 0.61×0.61 m with a length of 1.23 m, and is fitted with 0.66-m-diam optical glass windows [5,11,13]. These experiments were performed with a freestream Mach number of 2.3 and a stagnation pressure of 60 ± 3 kPa.

The cavity model used here has been the subject of recent experimental investigations by Schmit et al. [5,11,13]. The cavity has a length-to-depth ratio $L/D = 5.67$, with a streamwise length $L = 215.9$ mm and a width of 63.5 mm. The smooth flat-plate forebody is 177.8 mm in the streamwise direction and 127 mm in the spanwise direction, and the cavity is centered in the spanwise direction. The cavity sidewalls are made of optical-quality fused silica. The model is mounted on a crescent-shaped sting with a pitch angle of -3 deg. This angle results in an oblique shock wave attached to the model leading edge, which changes the freestream conditions over the cavity to Mach 2.18 with $U_\infty = 542$ m/s.

The flowfield is observed to undergo laminar to turbulent transition over the cavity opening under the present test conditions. While this does not represent most high-speed cavities in flight, these test conditions were nonetheless useful for the present purposes of describing new optical diagnostic techniques and analysis procedures.

A. Integrating Schlieren Optics

The TGF has a permanently installed z -type schlieren system with two 0.91-m-diam $f/5$ parabolic mirrors. This system was used to perform schlieren and shadowgraph imaging using a 350 W mercury-xenon compact-arc-lamp light source. High-speed images were recorded using a Photron SA-1 high-speed digital video camera with a $1 \mu s$ frame exposure at all frame rates. Still color schlieren images were recorded with a blue-yellow horizontal color cutoff using a Nikon D90 digital SLR camera with a $250 \mu s$ exposure time.

The low-speed color schlieren imagery has limited usefulness for quantitative data, as many interesting flow phenomena occur at a significantly faster timescale, and are thus blurred in the image. The low-speed image mainly reveals flow features that are steady, and it is useful in the traditional qualitative sense of giving a physical picture of the flowfield.

The low-speed image shows the presence of thermal noise outside the tunnel test section, but in the optical path. This thermal noise is observed as the irregularities in the background of the image (Fig. 1a). This noise can also be observed in the high-speed imagery as background irregularities, but these are neglected in quantitative measurements because they remain almost stationary during short measurement intervals.

The high-speed shadowgram in Fig. 1b shows the general flow features of the cavity-model flow at a single instant in time. The region of interest for the current work is the cavity and especially its shear layer. The shadowgraph technique is used here to emphasize regions of sharp contrast, such as shock waves and turbulent structures [7].

Note that there are also sidewall boundary layers on the wind-tunnel test section and the cavity optical windows. Optical distortions from these are averaged out in the low-speed images, but in the high-speed images, the sidewall boundary layers contribute to the background noise. It is difficult to identify which distortions are inside vs outside the tunnel using standard integrating optics.

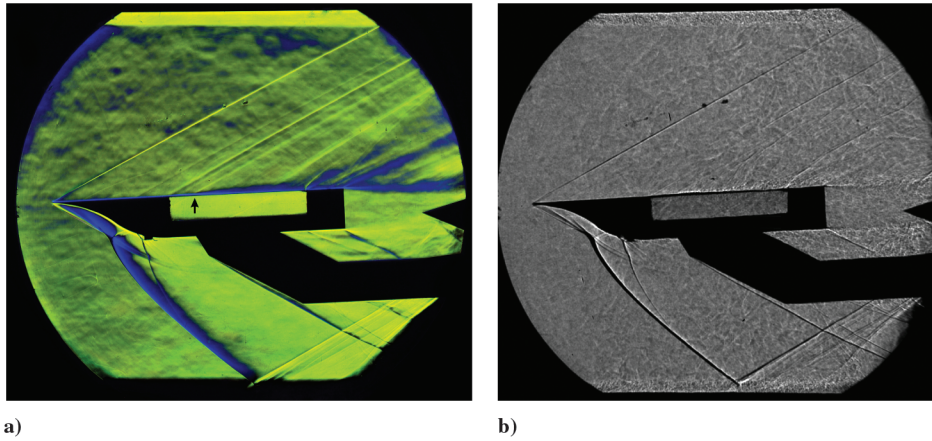


Fig. 1 Cavity model a) low-speed color schlieren image and b) high-speed shadowgraph image. The average transition location over the cavity is marked with the arrow in a).

B. Focusing Schlieren Optics

Focusing schlieren optics [7,14] are used here to image refractive disturbances within a limited depth of focus inside the wind-tunnel test section, and to eliminate the interference of the external thermal noise and boundary layers on the tunnel windows. The system used here is shown schematically in Fig. 2. The location of the depth of focus is moved within the test section by translating the entire rail-mounted optical system or by adjusting the focus of the camera lens. The depth of focus of this system was measured to be approximately ± 40 mm. For more details on the design and application of focusing schlieren optics for high-speed flows, see [12,15].

C. Light-Emitting-Diode Illuminator

A pulsed light-emitting-diode (LED) array was developed for use with the focusing schlieren system to allow imaging with a high-resolution TSI 11 megapixel camera, typically used for PIV. The electronic shuttering of this camera requires that two sequential images are individually exposed using a pulsed light source. The present LED array is an improvement on that previously presented by Hargather et al. [12]. It contains 16 LEDs (15 W, model LZ400CW15 from LedEngin) arranged in a four-by-four array. The LED drive circuit is shown schematically in Fig. 3, which represents one of the four identical circuits required to drive all 16 LEDs. The circuit is

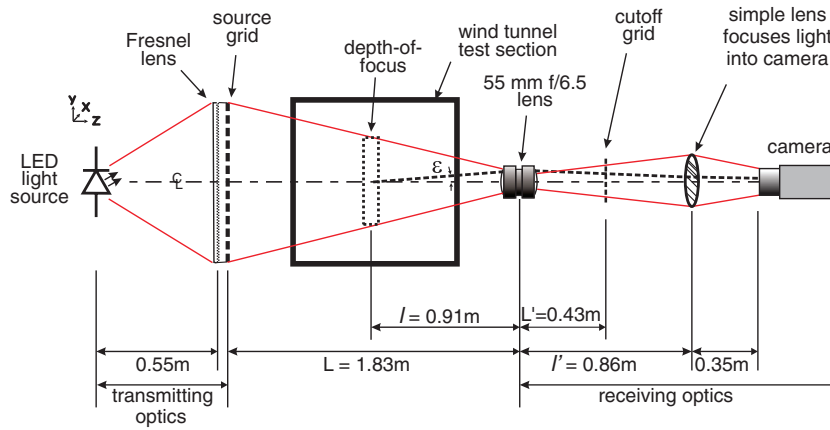


Fig. 2 Schematic of the focusing schlieren optical system.

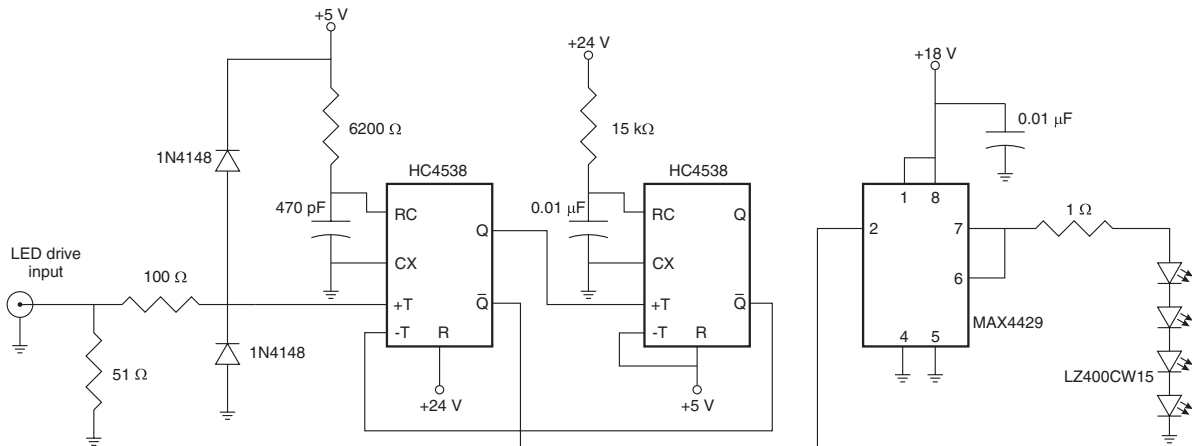


Fig. 3 Schematic of the LED array for driving one set of four LEDs.

controlled by the LED drive input, a transistor-transistor logic (TTL) high pulse with a duration equal to the desired duration of the light output. The light durations explored here varied from 0.5 to 4 μs . The LED-array illumination rise and fall times were measured to be approximately 0.05 μs using a photodiode. The array was double-pulsed by applying two consecutive TTL pulses, thus providing the required double exposure. The integrated-chips HC4538 and MAX4429 can be purchased, for example, from Mouser Electronics, part numbers 511-M74HC4538T and 700-MAX4429EPA, respectively. For further information on LED drivers for high-speed schlieren imaging, see [16].

III. Experimental Results

A. High-Speed Time-Resolved Shadowgraph Imaging

Using the TGF z -type schlieren system and the Photron SA-1 camera, high-speed shadowgraph images of the cavity flowfield were obtained. This revealed that the boundary layer on the cavity forebody is laminar and transitions to a turbulent shear layer over the cavity. Figure 4 shows a series of shadowgrams of the cavity flowfield. The shadowgrams are separated by 80 μs , the freestream flow is from left to right, and only the cavity itself is shown here. The transition to turbulent flow can be clearly observed in Fig. 4, in which the shear-layer thickness suddenly grows, and turbulent-flow structures can be observed. The convergence of the laminar shadow leading up to transition is as described and explained in [17].

The cavity oscillation cycle shown in Fig. 4 begins in a) and progresses to d). Image e) is at approximately the same point in the oscillation cycle as a). The most easily identifiable phenomenon within the cycle is the motion of the oblique shock wave at the leading edge of the cavity, which appears to lift above the cavity, then reforms at the cavity leading edge in e). The arrows in each image identify the approximate location of the shear-layer laminar-to-turbulent transition. The oblique shock wave at the cavity trailing edge also oscillates as turbulent structures impinge on the cavity rear wall.

The average laminar-to-turbulent transition location is also observed in the low-speed schlieren image in Fig. 1a. The transition point is indicated in the image with an arrow and can be identified by the weak shock wave that appears to emanate from that point. The rapid growth of the shear layer downstream of transition is responsible for this shock wave. The average transition location was found to be approximately 37 ± 1 mm downstream of the cavity leading edge, at about 17% of the cavity length.

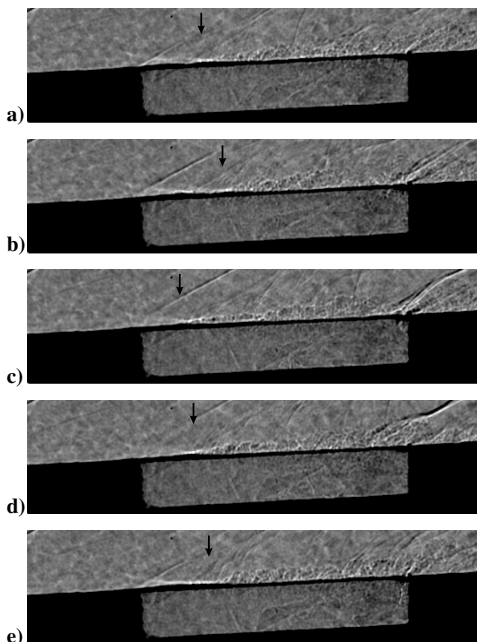


Fig. 4 Shadowgrams images of the cavity flowfield, separated by 80 μs intervals.

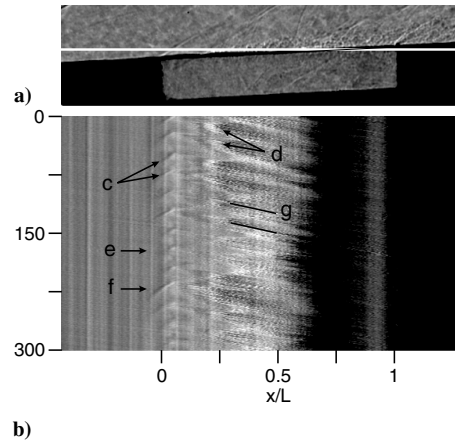


Fig. 5 a) A single row of pixels (highlighted in white) is extracted from each frame of the high-speed digital-image sequence, and is stacked vertically to create b) a streak image.

Digital streak images ($x-t$ or wave diagrams) were created from the high-speed digital video sequences. These pseudostreak images were created by extracting a single row of pixels from each image, and stacking the selected pixel rows to form a single image with time represented by the vertical axis [18]. Figure 5a shows a single shadowgram with the extracted pixel row highlighted by a white horizontal line. Figure 5b is the streak image formed from 300 sequential images, each separated by 13.3 μs , with time increasing in the downward direction. The images were recorded at 75,000 frames per second; thus, Fig. 5 represents 4 ms of time.

The streak image in Fig. 5b allows the visualization of the unsteady flow features of this cavity flow. The first observation is the regular oscillations of the oblique shock wave at the cavity leading edge. This shock motion, shown earlier in Fig. 4, is identified by (c) in Fig. 5b. The first row of pixels at the top of Fig. 5b is from the image in Fig. 5a. The shock-oscillation frequency is estimated from the streak image to be about 3200 ± 100 Hz.

Figure 5b also allows the visualization of the changing location of the laminar-to-turbulent transition. The transition itself is not directly imaged, but instead, the location where the turbulent shear-layer spreading has encountered the chosen pixel row (d). The transition point generally oscillates at the same frequency as the cavity-leading-edge shock wave. Two noticeable deviations are identified at (e) and (f). These deviations are accompanied by changes in the shock wave: as transition moves aft, the cavity-leading-edge shock wave weakens, and as transition moves forward, the shock becomes stronger.

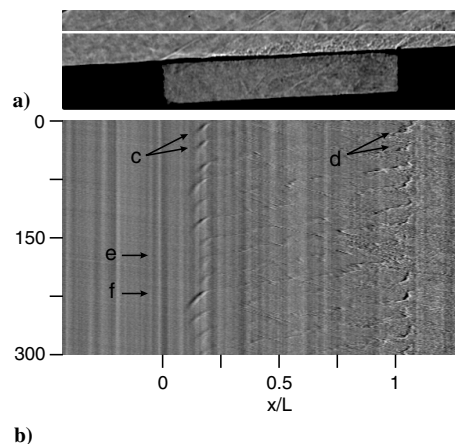


Fig. 6 a) Shadowgram with the row of pixels that is extracted to create b) the streak image. This image reveals the cavity c) leading-edge shock and d) trailing-edge shock. The marks e-f are at the same position as in Fig. 5.

The concept of SIV is also illustrated in Fig. 5b by following identifiable structures in the steak image, which make diagonal streaks (g) as they move downstream.

Figure 6 is created from a pixel row that is higher above the cavity, and thus shows the oscillations of the shock waves at both the leading and trailing edges of the cavity. An analysis of Fig. 6 shows that the frequency of the two shock oscillations is approximately the same, and that they are roughly in phase.

The streak images demonstrate the basic concept of the SIV [12]. In the turbulent-flow region, there are several identifiable diagonal lines [(g) in Fig. 5b)] that show the propagation of individual turbulent features downstream. Weak disturbance waves are also observed in Fig. 6b moving downward and to the left, indicating information propagating upstream. This is the upstream propagation of shock waves produced from the impingement of structures on the rear cavity wall, as initially sketched and described by Rossiter [1]. Such results could be improved by adjusting the camera mount so that the cavity top surface is aligned parallel to the pixel rows of the image sensor.

The high-speed images were also analyzed to determine the spreading rate of the shear layer after transition. The spreading angle was measured for many different images and transition locations, and was found to be about 6 ± 1 deg (half-angle) on average.

A Fourier analysis was performed on the high-speed shadowgraph-image sequence to identify the dominant frequencies in the images. This analysis performed a fast Fourier transform (FFT) on each pixel in the image as if it was a single photodiode, as previously done by Garg and Cattafesta [8]. Two thousand images, recorded at 75,000 frames per second, were analyzed in this way, providing a frequency resolution of $\Delta f \approx 37$ Hz.

Figure 7 visualizes the frequency data that were extracted from the image sequence across two different pixel rows. The pixel rows chosen in Figs. 7a and 7b are the same as those in Figs. 5 and 6, respectively. The dominant features of Figs. 7a and 7b are the shock waves at the leading and trailing edges of the cavity. These flow features oscillate at a discrete frequency, which is measured to be 3150 Hz, and is marked in the image with an arrow.

Broadband acoustic noise is observed radiating from the cavity, both vertically and slightly upstream. The frequency of each of these bands is estimated from the plots and given in Table 1. The error in the optical-frequency measurements is approximately $\pm 2\Delta f = \pm 74$ Hz. The optically measured oscillation frequencies are compared to the modified Rossiter cavity frequencies [19], f_n , and a closed-box oscillation frequency [19,20], f_b , in Table 1. The observed frequencies agree well with the closed-box frequencies.

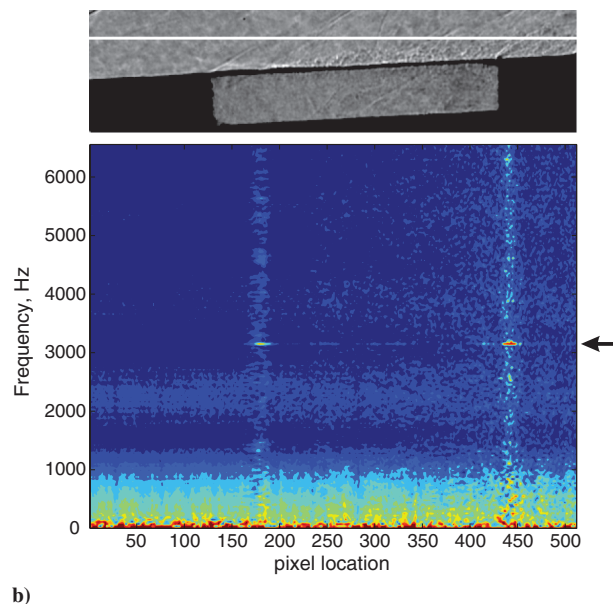
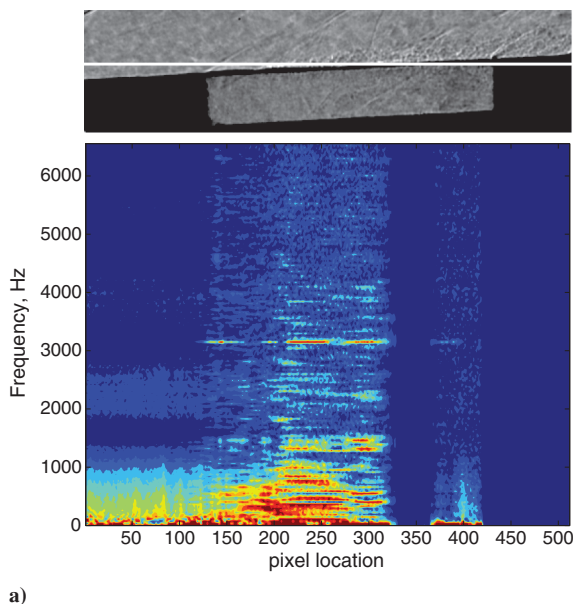


Fig. 7 Frequency spectra for individual lines from the high-speed video records.

Table 1 Cavity-oscillation frequencies

Mode number	Modified Rossiter f_n , Hz	Closed box f_b , Hz	Present optically measured, Hz
1	560	781	—
2	1307	1562	1400
3	2053	2344	2270
4	2800	3125	3150
5	3546	3906	3920
6	4293	4687	—
7	5039	5469	5600
8	5786	6250	—

The low-frequency range of the spectrum plots in Fig. 7 shows a high level of broadband noise and precludes the measurement of distinct frequency bands below 1000 Hz. This noise is attributed to the tunnel sidewall boundary layer and the thermal noise outside the tunnel, which are overlaid on these shadowgrams due to the integrating nature of the optics.

The frequency content of the flowfield can also be examined by plotting the FFT intensity at specific frequencies. Figure 8 is a set of intensity images showing the frequency content across the field of view at specific frequencies identified by mode numbers $n = 2 - 5$. The intensity has been normalized by the maximum intensity in the $n = 4$ image. The bottom image in Fig. 8 is at a frequency halfway

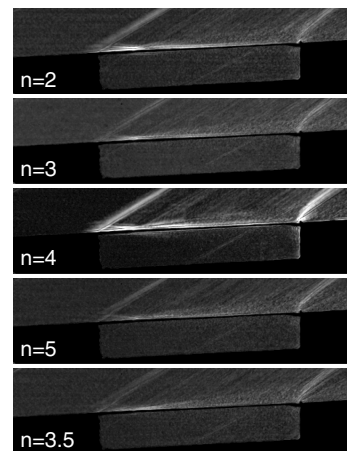


Fig. 8 Images showing the intensity of the frequency content throughout the observed field of view for various optically measured mode numbers.

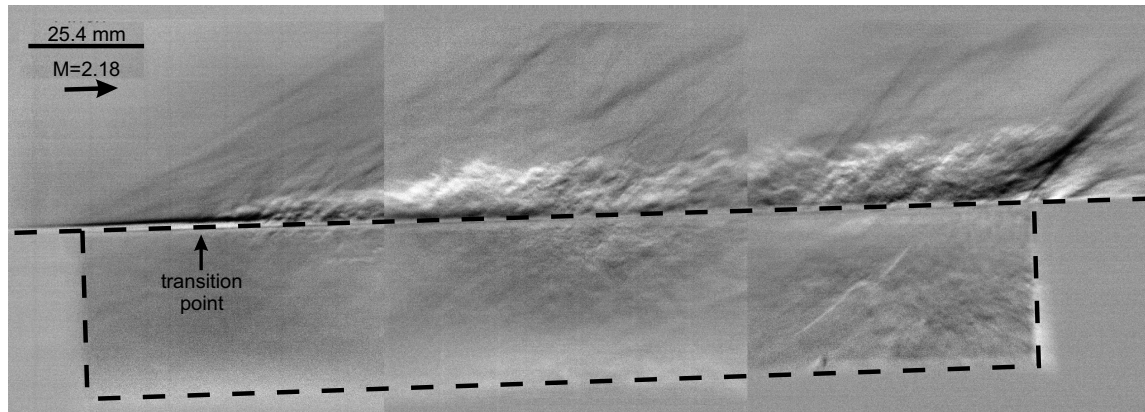


Fig. 9 Composite focusing schlieren image of the cavity flowfield.

between modes 3 and 4, and is presented as a control for an estimation of the amount of noise in this measurement. Only the images for $n = 2$ and $n = 4$ show a significantly higher frequency content than the control image. The dominant regions of the frequency content are the shock waves at the cavity leading and trailing edges, and the shear layer itself, especially near the transition location. It is not surprising that the transition region contains a significant frequency content at the same $n = 4$ frequency as the shock-wave oscillation, as it was already observed from the streak images that transition oscillates in phase with the shock-wave motion. The $n = 4$ image also shows a concentration of energy at the back wall of the cavity. The $n = 1$ mode is not shown here because there was significant noise at that frequency, which precluded the measurement of the mode frequency.

B. Focusing Schlieren Imaging

The focusing schlieren system was focused on the cavity centerline and used to image the cavity shear layer. This system blurs all refractive disturbances outside the depth of focus so that they are effectively not imaged, including the wind-tunnel sidewall boundary layers, the thermal noise outside the wind tunnel, and any flow features on the sides of the cavity model. A typical composite image of the cavity flowfield from the focusing schlieren system is shown in Fig. 9. This composite image is composed of three different images, which were required due to the limited field of view of the focusing schlieren system. The composite image was constructed from individual images that are from approximately the same time in the transition-location oscillation cycle; thus, the shear-layer spreading rate across the composite image is consistent.

The SIV was attempted on a series of images recorded using the focusing schlieren optics, but this nonstationary cavity flow precluded an accurate measurement of the shear-layer velocity profile given the limited data set that was recorded. The results clearly showed the potential for quantitative SIV velocity profiles from sequences of high-speed records such as Fig. 9, but the results await future work.

IV. Conclusions

Optical diagnostics of a supersonic transitional cavity shear layer were performed using high-speed shadowgraph imaging and a focusing schlieren optical system. The high-speed shadowgraph imaging was used to perform time-resolved flowfield measurements. Digital streak images were also produced from the high-speed digital-image series. The streak images were useful for identifying wave phenomena and their spatiotemporal propagation and oscillations.

A frequency analysis was performed on the digital-image series to determine the spectral content of the flowfield. Several peaks in the spectral-energy content were observed, which correlated well with predicted closed-box cavity-resonance frequencies. This analysis showed the dominant frequency to be approximately 3150 Hz, which is also the frequency at which the shock structures around the cavity were observed to oscillate. The cavity-shear-layer transition location

was observed to contain energy at a wide range of frequencies, especially including the shock-oscillation frequency.

The high-speed shadowgrams also identified thermal noise along the optical path, which led to the development of a focusing schlieren optical system for imaging refractive disturbances within a limited region. This system was used to image the cavity-shear-layer refractive-index field directly, and to defocus the appearance of all external refractive disturbances, including the tunnel sidewall boundary layers and freestream disturbances.

Schlieren and shadowgraph techniques, once mainly qualitative, are now readily combined with high-speed digital video recording, yielding large digital data sets. These open the possibility of a broad range of qualitative and quantitative optical measurements of unsteady, transitional, and turbulent refractive flows like the cavity flow studied here.

Acknowledgments

This work was funded by subcontract SB08-004 FA8650-08-C-3828 from Spectral Energies, LLC, based on a *Small Business Innovation Research* contract from the U.S. Air Force Research Laboratory, Wright-Patterson Air Force Base, monitored by Sivaram Gogineni. The authors would also like to thank the following for their support throughout this work: F. Semmelmayr, C. McGaha, J. D. Miller, L. J. Dodson-Dreibelbis, and R. A. Kreuter, who designed and built the light-emitting-diode illuminator.

References

- [1] Rossiter, J. E., "Wind-Tunnel Experiments on the Flow over Rectangular Cavities at Subsonic and Transonic Speeds," Aeronautical Research Council, Rept. and Memoranda No. 3438, London, Oct. 1964.
- [2] Cattafesta, L. N., Garg, S., Kegerise, M. S., and Jones, G. S., "Experiments on Compressible Flow-Induced Cavity Oscillations," AIAA Paper 98-2912, June 1998.
- [3] Bian, S., Driscoll, J. F., Elbing, B. R., and Ceccio, S. L., "Time Resolved Flow-Field Measurements of a Turbulent Mixing Layer over a Rectangular Cavity," *Experiments in Fluids*, Vol. 51, No. 1, 2011, pp. 51–63. doi:10.1007/s00348-010-1025-7
- [4] Zhuang, N., Alvi, F., Alkisar, M., and Shih, C., "Supersonic Cavity Flows and Their Control," *AIAA Journal*, Vol. 44, No. 9, 2006, pp. 2118–2128. doi:10.2514/1.14879
- [5] Schmit, R., McGaha, C., Tekell, J., Grove, J., and Stanek, M., "Performance Results for the Optical Turbulence Reduction Cavity," AIAA Paper 2009-702, Jan. 2009.
- [6] Cattafesta, L. N., Song, Q., Williams, D. R., Rowley, C. W., and Alvi, F. S., "Active Control of Flow-Induced Cavity Oscillations," *Progress in Aerospace Sciences*, Vol. 44, Nos. 7–8, 2008, pp. 479–502. doi:10.1016/j.paerosci.2008.07.002
- [7] Settles, G. S., *Schlieren and Shadowgraph Techniques: Visualizing Phenomena in Transparent Media*, Springer-Verlag, Berlin, 2001.
- [8] Garg, S., and Cattafesta, L. N., "Quantitative Schlieren Measurements of Coherent Structures in a Cavity Shear Layer," *Experiments in Fluids*, Vol. 30, No. 2, 2001, pp. 123–134. doi:10.1007/s003480000147

- [9] Zhuang, N., Alvi, F. S., and Shih, C., "Another Look at Supersonic Cavity Flows and Their Control," AIAA Paper 2005-2803, May 2005.
- [10] Alvi, F. S., and Cattafesta, L. N., "The Art and Science of Flow Control—Case Studies Using Flow Visualization Methods," *European Physical Journal Special Topics*, Vol. 182, No. 1, 2010, pp. 97–112.
- [11] Schmit, R. F., Semmelmayr, F., Haverkamp, M., and Grove, J. E., "Analysis of Cavity Passive Flow Control Using High Speed Schlieren Shadowgraph Images," AIAA Paper 2012-0738, Jan. 2012.
- [12] Hargather, M. J., Lawson, M. J., Settles, G. S., and Weinstein, L. M., "Seedless Velocimetry Measurements by Schlieren Image Velocimetry," *AIAA Journal*, Vol. 49, No. 3, 2011, pp. 611–620. doi:10.2514/1.J050753
- [13] Schmit, R. F., Semmelmayr, F., Haverkamp, M., and Grove, J. E., "Fourier Analysis of High Speed Shadowgraph Images Around a Mach 1.5 Cavity Flow Field," AIAA Paper 2011-3961, June 2011.
- [14] Weinstein, L., "Large-Field High-Brightness Focusing Schlieren System," *AIAA Journal*, Vol. 31, No. 7, 1993, pp. 1225–1250.
- [15] Weinstein, L. M., "Review and Update of Lens and Grid Schlieren and Motion Camera Schlieren," *European Physical Journal Special Topics*, Vol. 182, No. 1, 2010, pp. 65–95.
- [16] Willert, C. E., Mitchell, D. M., and Soria, J., "An Assessment of High-Power Light-Emitting Diodes for High Frame Rate Schlieren Imaging," *Experiments in Fluids*, Vol. 53, No. 2, 2012, pp. 413–421. doi:10.1007/s00348-012-1297-1
- [17] Chapman, D. R., Kuehn, D. M., and Larson, H. K., "Investigation of Separated Flows in Supersonic and Subsonic Streams with Emphasis on the Effect of Transition," NACA TR-1356, 1958.
- [18] Katayama, A. S., "Visualization techniques for temporally acquired sequences of images," US Patent No. 5294978, 1994.
- [19] Unalms, O. H., Clemens, N. T., and Dolling, D. S., "Cavity Oscillation Mechanisms in High-Speed Flows," *AIAA Journal*, Vol. 42, No. 10, 2004, pp. 2035–2041. doi:10.2514/1.1000
- [20] Heller, H. H., Holmes, D. G., and Covert, E. E., "Flow-Induced Pressure Oscillations in Shallow Cavities," *Journal of Sound and Vibration*, Vol. 18, No. 4, 1971, pp. 545–553. doi:10.1016/0022-460X(71)90105-2

G. Elliott
Associate Editor